



Al Alloy Tailor Welded Blank Fabrication by Friction Stir Welding: Effect of Double-Pass

Tanveer Majeed, Yashwant Mehta, and Arshad Noor Siddiquee

Submitted: 7 April 2021 / Revised: 16 June 2021 / Accepted: 17 July 2021 / Published online: 30 August 2021

Friction stir welding (FSW) in butt joint configuration between 6.35 mm thick plates of AA2024-T3 and 2.5 mm thick plates of AA7475-T7 dissimilar alloys is addressed using T4 tool steel with a tapered cylindrical pin having scrolled shoulder. In this experimental study, the effect of double-pass FSW on joint properties has been investigated in detail. The weld microstructure and mechanical properties of FSWed joints were characterized. Scanning electron microscopy and x-ray energy-dispersive spectroscopy were employed to analyze the distribution and nature of precipitates. The temperature rise and traverse load during the FSW process were evaluated. Experimental results indicated the significant increase in grain size by double-pass FSW. Moreover, the hardness value decreases with the second pass, and the hardness dropped significantly in the heat-affected zone due to grains coarsening and change in precipitate morphology caused by increased heat input by double-pass FSW. The overall reduction in joint strength was found to be 4.8% by second pass FSW.

Keywords aluminum alloy, double-pass, friction stir welding, microstructure, microhardness, temperature analysis

1. Introduction

The current trend toward lightweight design is directed to reduce fuel consumption. Aluminum alloys (Al alloys) have evolved as the leader in weight reduction due to high specific strength and corrosion resistance. Consequently, alloys of Al are replacing steel in aerospace, armor, locomotive, and shipbuilding industries (Ref 1). Al alloys from AA2xxx and AA7xxx series are widely employed in aerospace, armor, and railroad components (Ref 2). The AA2xxx and AA7xxx series alloy are age-hardenable and attain optimal tensile strength, toughness, and corrosion resistance due to Al_2Cu and $MgZn_2$, Al_2Cu and Al_2CuMg , respectively (Ref 3, 4). However, the unfavorable change in precipitate morphology at higher temperatures is the major issue during fabrication. These challenges can be met by the solid-state welding technique known as the friction stir welding (FSW). In FSW, the materials are joined by applying frictional adiabatic heat and stirring the hot-softened material by a non-consumable rotating tool (Ref 5). During FSW, the tool while rotating is also traversed along the welding direction causing material consolidation to complete the joint.

It is always beneficial to develop prefabricated structural members rather than producing them on sight. The prefabricated components are mostly produced by joining different

materials in desired thicknesses in various joint configurations (such as butt, lap, T joints, etc.) and are all collectively known as Tailor Welded Blanks (TWBs). The TWBs comprising of members with unequal thickness made from similar/dissimilar material find a wide range of applications in aeronautical, armor, and transportation sectors and have resulted in great savings in weight and production time as high as 50% (Ref 6). However, the fabrication of TWBs by joining dissimilar material combinations is highly challenging due to a mismatch in the properties of the dissimilar materials. Multi-pass welding is a very commonly employed strategy to achieve better consolidation. But, in the case of age-hardened alloys, it often proves counterproductive.

Double-pass FSW was found to improve the strength and elongation for several alloys such as AA6061 and AA1xxx (Ref 7, 8). When one or both alloys are age-hardened, the multi-pass strategy may cause softening due to overaging and grain growth in the heat-affected zone (HAZ) (Ref 9). In the case of age-hardened materials (such as AA7050-T7), multiple passes have been found to reduce the joint strength (Ref 10). While single-pass welds in thick plates produce a large thermal gradient in the thickness direction, double-sided (two pass) FSW may enhance heat input which may cause more harm than benefit in the case of age-hardened alloys. Although double-sided FSW has reportedly enhanced the joint strength in some cases such as in FSW of similar 8 mm thick AA6082-T6 plates and 6 mm thick AA19000-H12 plates (Ref 11, 12). Typically for AA6061, the second pass FSW resulted in decreased mechanical properties, whereas the double-sided second pass FSW significantly improved the properties (Ref 13). The double-sided weld on 15 mm thick AA6063 FSW joints was found to possess better fatigue crack propagation rate (Ref 14). Furthermore, the double-pass FSW between AA2024 and Ti-6Al-4V was found to increase the joint strength by 17.3% and elongation by 1.6% (Ref 15). The addition of Cu powder between AA6061 and AA7075 during double-pass FSW is found to significantly enhance material flow and grain refinement in the weld nugget (WN) (Ref 16).

Tanveer Majeed and **Yashwant Mehta**, Department of Metallurgical and Materials Engineering, National Institute of Technology, Hazratbal, Srinagar 190006 Jammu and Kashmir, India; and **Arshad Noor Siddiquee**, Department of Mechanical Engineering, Jamia Millia Islamia, New Delhi 110025, India. Contact e-mail: tanveer_02phd18@nitsri.net.

Generally, the welding between similar/dissimilar materials having unequal thicknesses is more difficult, expertise dependent, and often forces a practitioner to employ multiple pass welding. But in the case of age-hardened materials, the multi-pass strategy requires utmost diligence, becomes very much expertise dependent, and yet may prove counterproductive. The softening in AA2xxx and AA7xxx series, however, can be controlled by FSW provided that the welding is performed with diligence (Ref 17). The thickness of the alloys at the interface in the TWBs is often different; this makes dissimilar material welding having unequal thickness very useful. The multi-pass strategy is well investigated for similar and dissimilar materials by joining mostly in equal thickness combinations. In case of unequal thicknesses, it is challenging and the joint properties severely decrease with increasing thickness ratio especially for age-hardened alloys. The literature on welding of unequal thicknesses is very less reported, with only one study on plate thickness ratio of 2 between similar materials (Ref 18). As a matter of fact, the effect of double-pass on joint properties in TWBs of dissimilar Al alloys has not yet been reported.

The welding between AA2xxx and AA7xxx in unequal thickness combination is not claimed; FSW of unequal thickness dissimilar alloys for plate thickness ratio greater than 2 has not yet been reported and has wide applications in the aerospace industry such as aircraft fuselage, stringers, and wings (Ref 19). The effect of double-pass on the joint quality of age-hardened alloys is often contradicting. Present work has made a maiden attempt to investigate and compare single-pass and double-pass FSW welds between unequal thickness dissimilar Al alloys (AA2024-T3 and AA7475-T7), having a plate thickness ratio of 2.54. The influence of single-pass and double-pass FSW on microstructure, mechanical properties of joints and distribution of precipitates across the weld cross-section have been explained in detail.

2. Materials and Experimental Methods

TWBs were fabricated via FSW between dissimilar Al alloys (6.35 mm thick AA2024-T3 plates and 2.5 mm thick AA7475-T7 plates) in butt joint configuration. The AA2024-T3 and AA7475-T7 plates of dimensions 180 x 55 x 6.35 mm and 180 x 55 x 2.5 mm, respectively, were used as base materials (BMs). The chemical composition of both alloys was determined by x-ray fluorescence spectroscopy and the experimentally measured values of mechanical properties of AA2024-T3 and AA7475-T7 base alloys are given in Tables 1 and 2, respectively.

The welding was performed on a vertical milling machine adapted to perform FSW (refer Fig. 1). The welding was performed in the bottom flat position (BFP) with tool tilt angle (α) = 2° and inclination angle (θ) = 10° of the plate's surface with the XY plane of the machine table. The inclination angle (θ)

was provided to compensate for the difference in thickness between the BM plates. Figure 1a shows the experimental setup used to perform FSW. Before welding, the BM plates were machined and cleaned with acetone to remove the tenacious surface oxide layers. During welding, the AA2024-T3 plates were placed on the advancing side (AS) and AA7475-T7 plates on the retreating side (RS) as shown in Fig. 1(c). This arrangement makes the deposition of material from thicker plate (AA2024-T3) to thinner plate (AA7475-T7) effective. The FSW was performed with T4-tool steel, having tapered cylindrical pin, and scrolled shoulder as shown in Fig. 1(b). During FSW, the temperature data were acquired from eight locations by installing eight K-type thermocouples (as shown in Fig. 1(a) and (c)). The variation of traverse force (F_x) was also measured using a load cell attached to the FSW fixture (Fig. 1a). After FSW, the specimens for tensile testing, microhardness, and microstructural characterization were machined from welded plates across the transverse direction by using a wire electric discharge machine (WEDM). The standard metallographic procedure was followed for polishing the specimens which were subsequently etched with standard Keller's reagent for 12s. The macrostructure and microstructure of welded specimens were obtained using a stereoscope viewer and scanning electron microscope (SEM), respectively. The schematic of the tensile specimen along with the required dimensions is shown in Fig. 2(a). Tensile testing was performed according to ASTM E8M-04 using a computer interface tensometer at a crosshead speed of 2 mm/min. After failure, the fractured surfaces were examined by SEM. Vickers microhardness was measured (as per the scheme given in Fig. 2(b)) under a load of 30 gf, and indentations were made at 0.5 mm equidistant points at a dwell time of 15s.

3. Results and Discussion

The FSW process parameter conditions as indicated in Table 3 were optimized through a rigorous experiment regime. A total of 27 experiments were performed between unequal thickness dissimilar Al alloys using Taguchi L27 experimental array. After extensive investigations of the mechanical properties of all welded specimens, the specimen with the best overall mechanical properties was selected for further investigations. A detailed explanation of the whole process is illustrated in Fig. 3. The single-pass weld was made on the optimized parameter setting and a sound weld was obtained (Fig. 3a, b and c). The single-pass weld was allowed to cool naturally to room temperature. The double-pass welding was performed by overlaying the second pass immediately on the single-pass weld by following the same parameter setting (Fig. 3d,e and f). In the case of the first pass, the tool encountered a step at the faying surface (Fig. 3b) due to a mismatch in the thickness of two alloys. But, when the second pass (Fig. 3e) is made over

Table 1 Chemical composition of AA2024-T3 and AA7475-T7 base alloys (wt.%)

Alloy	Zn	Mg	Fe	Si	Cu	Zr	Cr	Mn	Ti	Ni	Al
AA2024-T3	0.02	1.10	0.204	0.074	4.57	...	0.005	0.51	0.04	0.014	Bal.
AA7475-T7	5.36	1.93	0.101	0.06	1.34	0.0076	0.155	0.0062	0.023	0.002	Bal.

Table 2 The measured values of mechanical properties of AA2024-T3 and AA7475-T7 base alloys

Alloy	UTS, MPa	Yield strength, MPa	Elongation, %	Hardness, HV
AA2024-T3	440	295	15	137
AA7475-T7	468	430	12	162

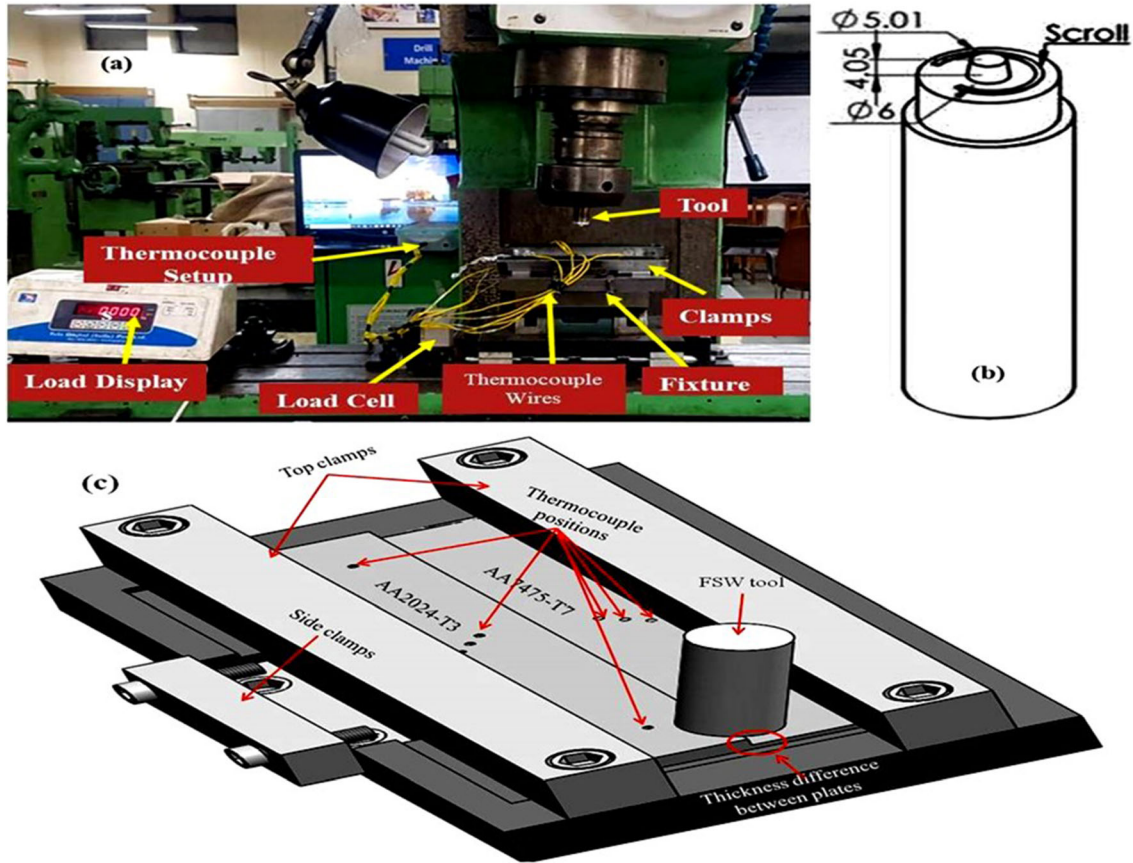


Fig. 1 (a) The experimental setup for FSW of TWBs, (b) The schematic representation of the FSW tool, and (c) The FSW experimental plan with thermocouple locations

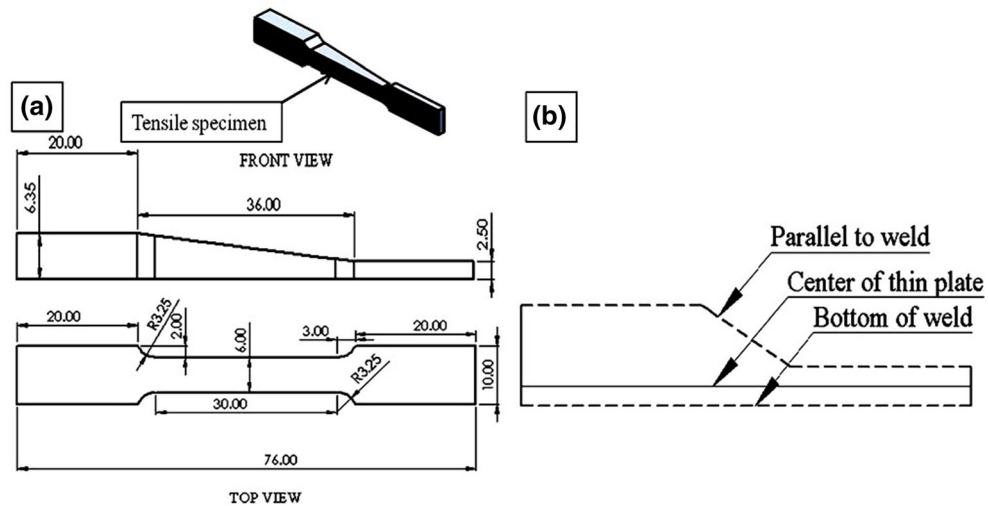


Fig. 2 Schematic of (a) Tensile specimen, and (b) Vickers hardness measurement at different locations

Table 3 Single and double-pass FSW parameters used in this investigation

Tool speed, rpm	rotational speed, rpm	Welding speed, mm/min	Shoulder size, mm	Pin Length, mm	Pin profile	Tool Tilt, α , degree	Tool inclination Angle, θ , degree
900		80	22	4.05	Taper cylindrical (Conical)	2	10

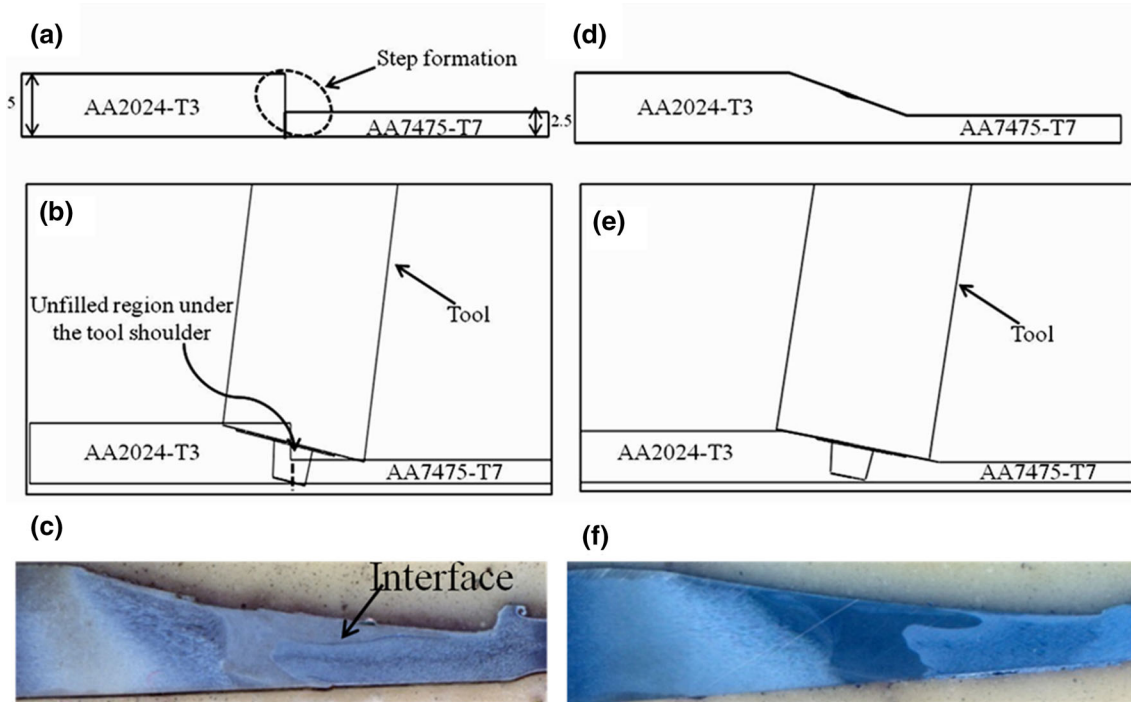


Fig. 3 (a) Schematic of the step formed due to unequal thickness FSW, (b) Schematic showing step encountered by FSW tool during first pass (pin partially submerged within BM), (c) Macrographs from the transverse section FSW weld after the first pass, (d) Schematic showing the step flushed out after first FSW pass, (e) Schematic of FSW tool pin fully submerged and the step not encountered by tool, and (f) Macrograph of a transverse section of FSW joint after double-pass

the preceding single-pass weld, the tool does not encounter the step, and the material flow from AS to RS is gradual and uniform.

3.1 Macro- and Microstructure Analysis

Figure 4 and 5 illustrates the macro- and micrographs of dissimilar material dissimilar thickness single-pass (DMDT-SP) and double-pass (DMDT-DP) FSWed joints, respectively. The macro-images indicate that defect-free joints are produced by both single and double-pass FSW. It can be noticed from the macrostructure of joint cross sections that an interface (Fig. 3c) is formed on RS between AA2024-T3 and AA7475-T7 alloys in single-pass FSW and the macrostructure is asymmetric. The interface disappears in the weld made with double-pass, and the macrostructure is homogenized and becomes symmetric. This is attributed to the fact that during the first pass the shoulder has to move the material from AS (i.e., thicker plate) to RS through a step and material flow is abrupt. The step is not present during the second pass which makes the material flow gradually and uniform and also the shoulder makes proper contact with the pre-welded surface produced by single-pass FSW.

Four characteristic zones were observed on either side of the centerline of weld cross section as shown in Fig. 4 and 5: the

BM, the heat-affected zone (HAZ), the thermomechanically affected zone (TMAZ), and the stir zone/weld nugget (SZ/WN). Locations 'A' and 'B' correspond to HAZ and TMAZ on AS, i.e., HAZA and TMAZA, respectively, whereas locations 'E' and 'F' correspond to TMAZ and HAZ on RS, i.e., TMAZR and HAZR, respectively (Fig. 4 and 5). The region 'C' in Fig. 4 and 5 represents SZ in single and double-pass welds. The visual difference in grain size in different weld zones can be also observed in Fig. 4 and 5. Figure 6 shows the variation of grain size of different weld regions of the DMDT-SP and DMDT-DP weld specimens. The grains in SZ are fine and equiaxed due to the strong stirring action of the tool and dynamic recrystallization (DRX) of grains as a result of high strain rates and frictional thermal cycles. It can be seen from Fig. 6 that in the DMDT-DP specimen, the grains in SZ/WN are moderately larger than the DMDT-SP specimen (Fig. 4) which is attributed to the increased heat input during double-pass FSW. The interface (Fig. 4, region D) between AA2024-T3 and AA7475-T7 in SZ can be observed in the DMDT-SP FSWed specimen represents the improper intermixing of materials at the interface. In the case of the DMDT-DP specimen (Fig. 5, region D), the homogenous mixing was observed as represented by the formation of onion rings at the interface of AA2024-T3 and

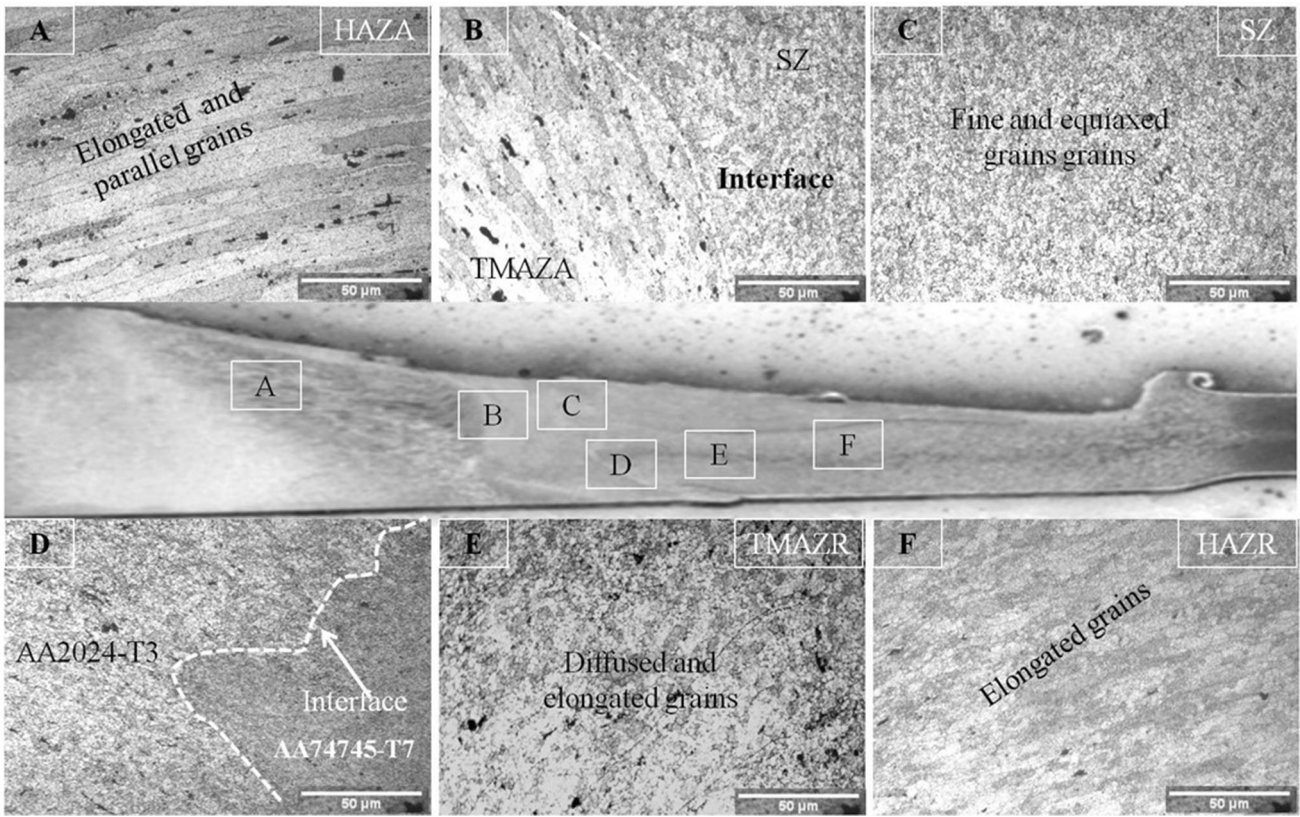


Fig. 4 Shows the macrostructure and microstructure of (a) Single-pass, and (b) Double-pass FSWed joints

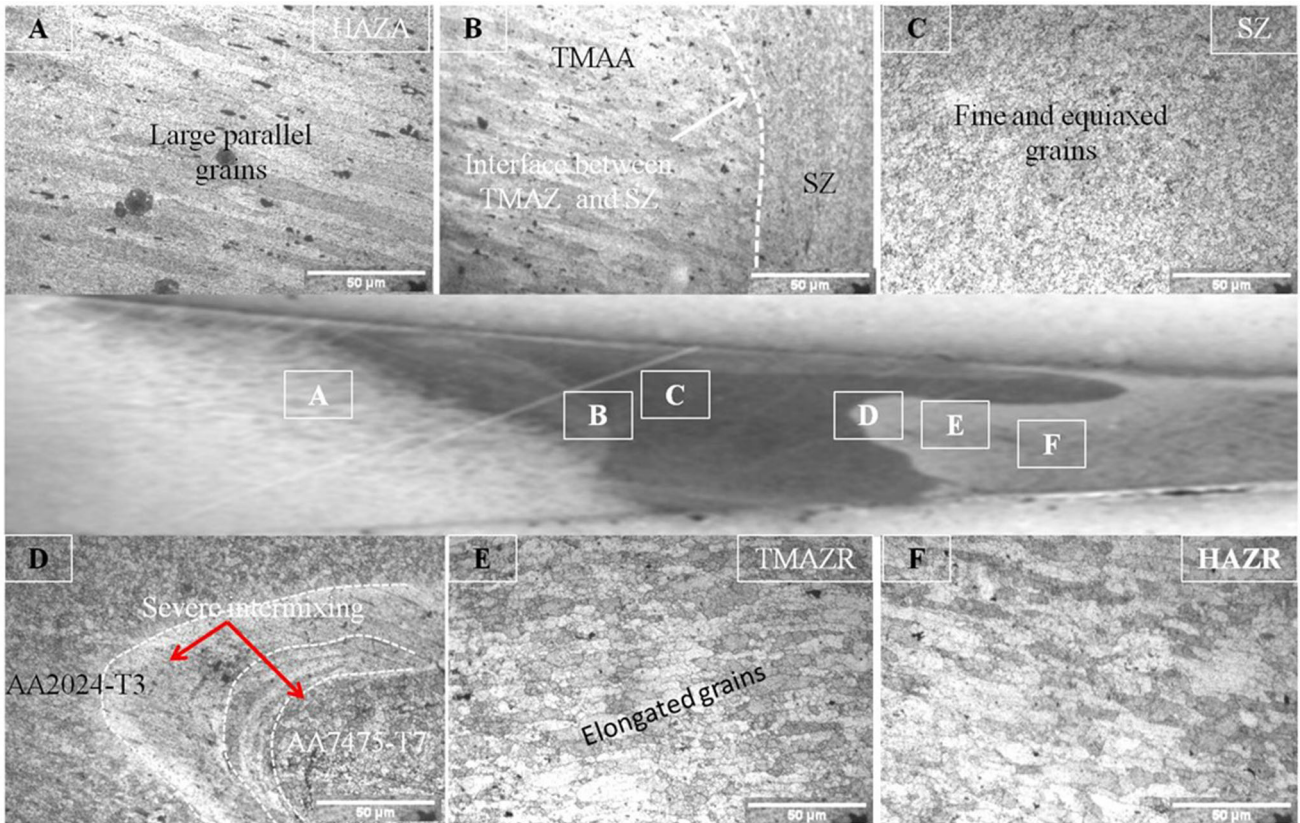


Fig. 5 Shows the macrostructure and microstructure of (a) Single-pass, and (b) Double-pass FSW joints

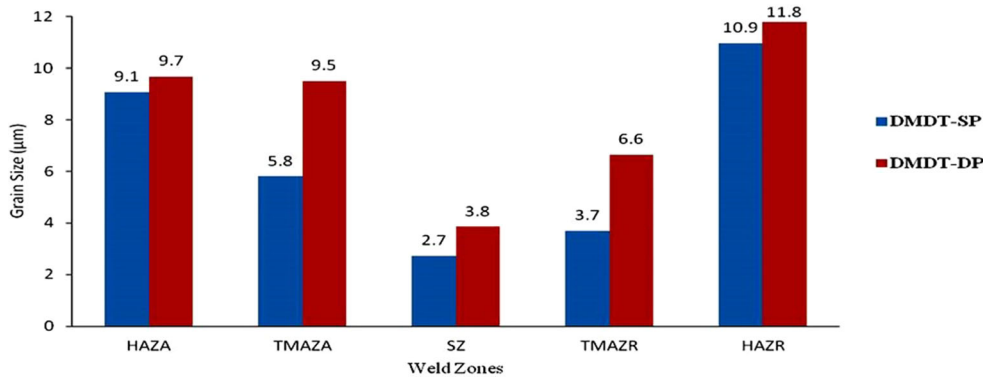


Fig. 6 Representation of grain size in different weld regions in a single-pass and double-pass FSW

AA7475-T7 in SZ attributed to the intense mixing and severe plastic deformation by double-pass FSW.

It can be observed from Fig. 6 that the grains are relatively bigger in SZ (3.8 µm) of double-pass weld in comparison to SZ (2.7 µm) of single-pass weld. This may be attributed to the increased heat input by double-pass FSW. On either side of SZ (i.e., in the TMAZ), the grains are bigger than those in SZ due to moderate thermal cycles and partial recrystallization during the FSW. Furthermore, the grains in TMAZ are elongated which characterize the material flow around the pin during welding. Moreover, it can be noticed from Fig. 4 and 5 that the grains in TMAZ of double-pass welds are moderately bigger (Fig. 5) and elongated in comparison to single-pass welds which is attributed to lower heat input and ineffective material flow around the tool pin and partial plastic deformation which consequently leads to increase in grain size. The TMAZ is surrounded by HAZ as shown in Fig. 4 and 5. The grains in HAZ are larger in size (Fig. 6) as compared to SZ and TMAZ due to the absence of plastic deformation and the presence of high thermal cycles leading to grain growth. Moreover, significant coarsening of grains can be observed in HAZ of double-pass weld due to high thermal cycles resulting from increased heat input by double-pass FSW. The coarsening effect is dominant in TMAZA and HAZR in both single and double-pass welds. This remarkable behavior is attributed to the presence of dissimilar materials having different metallurgical properties across the weld centerline and due to mismatch in thickness of the two alloys.

3.2 Scanning Electron Microscopic and X-ray Energy-Dispersive Spectroscopic Analysis

Figure 7 and 9 illustrates the SEM images of DMDT-SP and DMDT-DP weld specimens, respectively. Figure 8 and 10 shows the x-ray energy-dispersive spectroscopic (x-ray EDS) elemental mapping of single and double-pass joints, respectively. The SEM and x-ray EDS mapping was carried out to study the nature and distribution of precipitates and elemental composition of the second phase precipitates across the weld in single and double-pass joints. The x-ray EDS element maps of single and double-pass joints indicate the presence of Al and major alloying elements (such as Cu, Mg, Si in AA2024-T3 and Cu, Zn, Mg in AA7475-T7) (Ref 20).

X-ray EDS analysis of Cu-rich particles showed a wide range of elemental compositions in different weld regions (Fig. 8 and 10). Various second phase coarse particles obtained in different regions of single and double-pass welds are

represented in Table 4. The Fe-bearing particles show presence of CuFeMn in the range of 30-35 at.% and Al 65-75 at.%. This phase can be described as $(AlCu)_2(CuFeMn)$ (Ref 21). Basically, the phases originate from $Al_2(CuFeMn)$ containing 31.65 at.% CuFeMn and 68.35 at.% Al. In this case, the tendency of Cu atoms to replace Al atoms leads to the formation of $(AlCu)_2(CuFeMn)$ phase. X-ray EDS analysis of HAZR showed the presence of Zn bearing precipitates such as $(AlCu)_2(CuFeZn)$ (refer Fig. 7f) and $Al_3Cu_5(CuZnSi)$ derived from the equilibrium phase in BM (AA7475-T7) (Ref 21).

Figure 7 shows the SEM images of various single-pass weld zones. Figure 7(a), (b), (c), (d), (e) represents the microstructure of HAZA, TMAZA, SZ, TMAZR, and HAZR obtained from single-pass weld, respectively. Figure 8(a), (b), (c) and (d) and 7(f) shows the x-ray EDS analysis of HAZA, TMAZA, SZ, TMAZR, and HAZR obtained from single-pass joint, respectively. It was observed that Al_2CuMg was not present whereas rod-shaped fine $Al_2(CuFeMn)/(AlCu)_2(CuFeMn)$ precipitates were present in SZ. In contrast, x-ray EDS analysis (Fig. 8b and Fig. 7d) of second phase coarse precipitates reveal the presence of $Al_5Cu_8Mg_2$ in TMAZA and $(AlCu)(CuFeMn)$ in TMAZR. Figure 8(a) and 7(f) represents the x-ray EDS of coarser precipitates in HAZA and HAZR, respectively. It was revealed that such coarse particles were composed of Al_3Cu_6Mg in HAZA and $(AlCu)_2(CuFeZn)$ in HAZR. The increase in size and decrease in density of precipitates from SZ to TMAZ and then HAZ were due to the progressive decrease in the degree of plastic deformation as one moves from SZ to HAZ. The presence of small rod-shaped precipitates in SZ was attributed to severe plastic deformation and intense stirring in this region whereas the presence of coarse second phase precipitates in TMAZ and HAZ was attributed to lower temperature in these regions due to the partial plastic deformation (TMAZ) but sufficient enough to cause coarsening/aging of second phase precipitates. In addition, the difference in the nature and size of precipitates on AS and RS is due to dissimilar material combinations at the interface of joint and non-uniform heat distribution on AS (high heat input) and RS (lower heat input).

SEM images in Fig. 9 reveal the size and distribution of second phase particles in various weld zones. Figure 9(a), (b), (c), (d) and (e) represents the SEM images of HAZA, TMAZA, SZ, TMAZR, and HAZR of double-pass welds, respectively. On the other hand, Fig. 10(a), (b), (c), (d) and 9(f) represents the x-ray EDS of different weld zones evolved during double-pass FSW. X-ray EDS of spherical precipitates in SZ reveals the presence of $Al_2(CuFeMn)$ or $(AlCu)_2(CuFeMn)$ particles

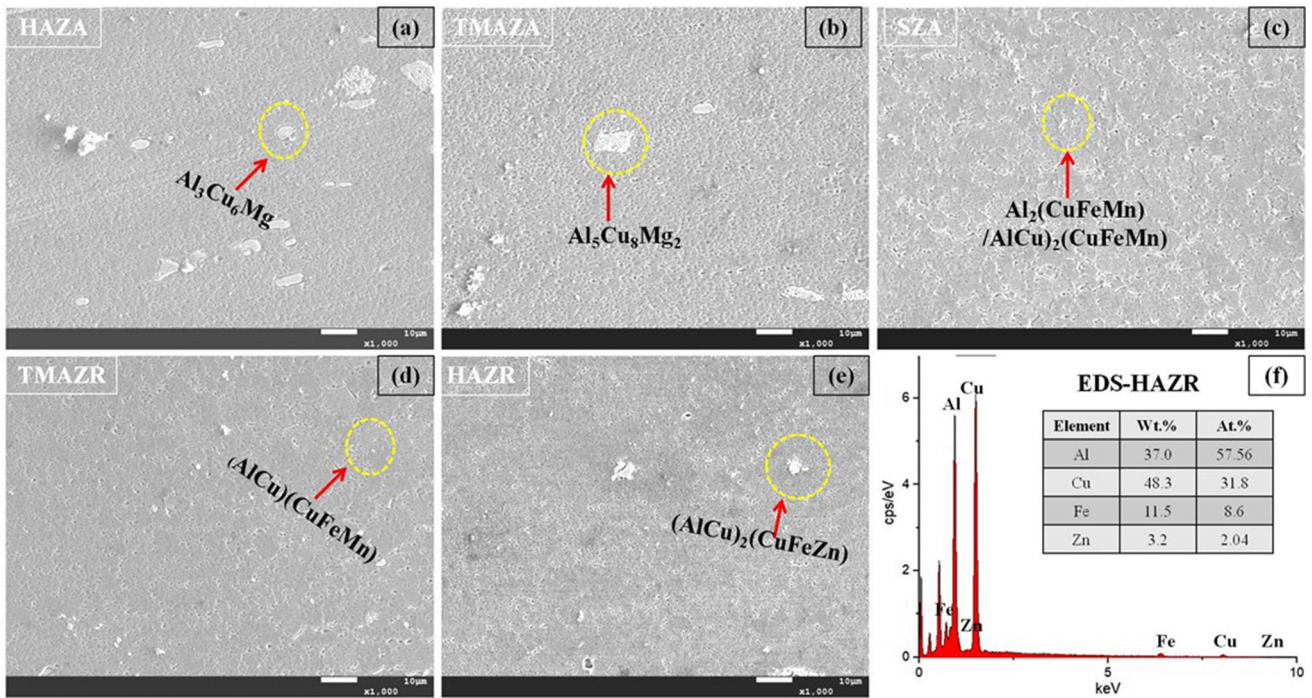


Fig. 7 SEM micrographs of (a) HAZA, (b) TMAZA, (c) SZ, (d) TMAZR, (e) HAZR and, (f) EDS elemental maps of HAZR

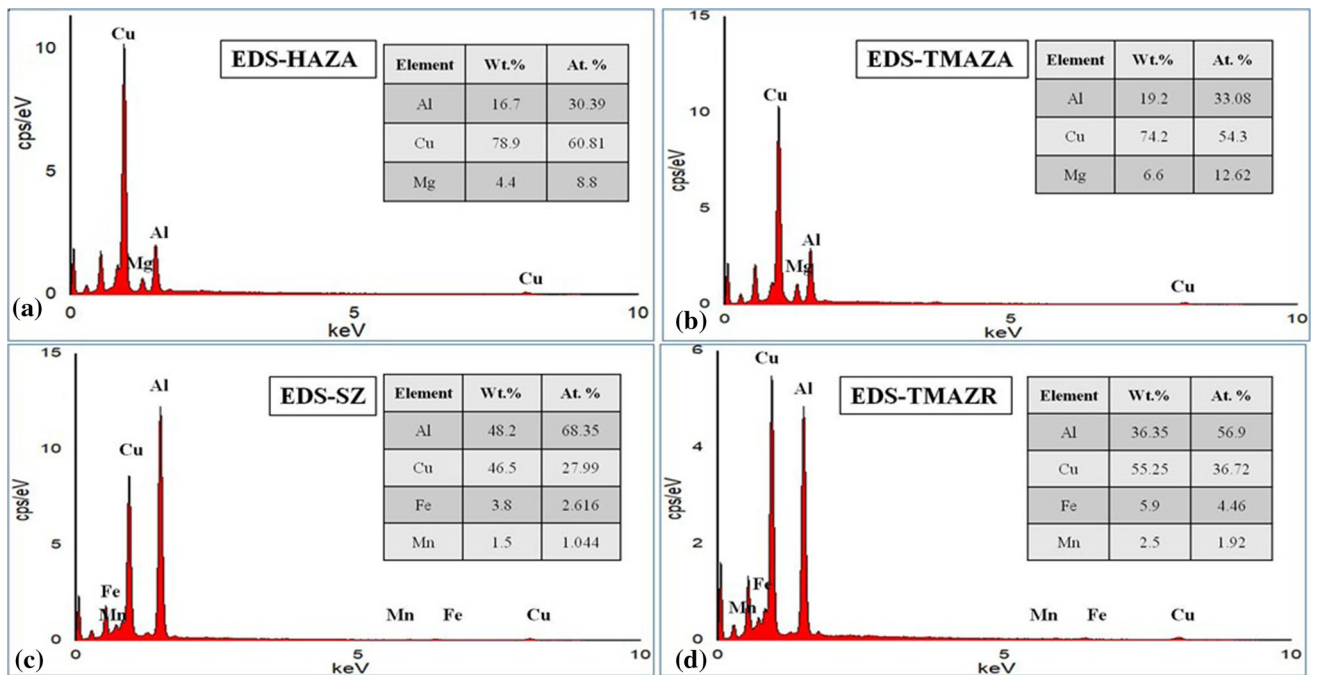


Fig. 8 EDS elemental maps of (a) HAZA, (b) TMAZA, (c) SZ and, (d) TMAZR of single-pass FSWed joints

(Fig. 10c). Figure 9(b) and (d) shows the SEM images of TMAZA and TMAZR and indicates the presence of coarse particles. It was observed from x-ray EDS (Fig. 10a and d) that coarse second phases composed of $\text{Al}_5\text{Cu}_8\text{Mg}_2$ and $(\text{AlCu})(\text{CuFeZn})$ were obtained in TMAZA and TMAZR regions, respectively. Whereas the presence of coarse plate shaped precipitates ($\text{Al}_3\text{Cu}_4\text{Mg}_2$) (Fig. 9a) and fine spherical shaped ($\text{Al}_3\text{Cu}_5(\text{CuZnSi})$) precipitates (Fig. 9e) were observed by x-ray EDS of HAZA and HAZR regions, respectively. The formation

of fine spherical precipitates in SZ of double-pass weld is attributed to the extreme plastic deformation and fragmentation of previously formed rod-shaped precipitates in single-pass weld. The presence of coarse precipitates in TMAZ and HAZ was attributed to lower temperature during the second pass but sufficient enough to cause coarsening of precipitates in TMAZ and HAZ.

SEM characterization of weld cross section (Fig. 6 and 8) indicates the formation of fine precipitates in SZ in single-pass

Table 4 Distribution and composition of coarse second phase particles produced during single and double-pass FSW

Characteristic weld zones	Second phase particles in SMDT-SP FSW specimen	Second phase particles in DMDT-DP FSW specimen
HAZA	$\text{Al}_3\text{Cu}_6\text{Mg}$	$\text{Al}_5\text{Cu}_5\text{Mg}_2$
TMAZA	$\text{Al}_5\text{Cu}_8\text{Mg}_2$	$\text{Al}_5\text{Cu}_8\text{Mg}_2$
SZ	$\text{Al}_2(\text{CuFeMn})/(\text{AlCu})_2(\text{CuFeMn})$	$\text{Al}_2(\text{CuFeMn})/(\text{AlCu})_2(\text{CuFeMn})$
TMAZR	$\text{AlCu}(\text{CuFeMn})$	$(\text{AlCu})(\text{CuFeMn})$
HAZR	$(\text{AlCu})_2(\text{CuFeZn})$	$\text{Al}_3\text{Cu}_5(\text{CuZnSi})$

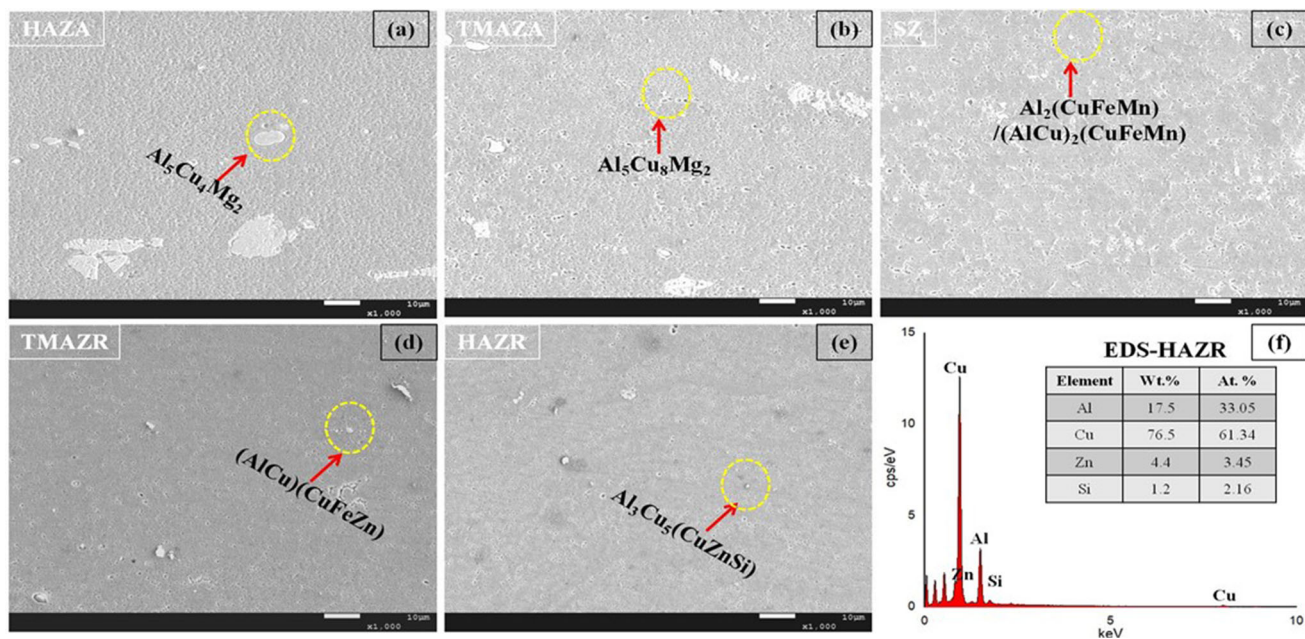


Fig. 9 SEM images of (a) HAZA, (b) TMAZA, (c) SZ, (d) TMAZR, (e) HAZR, and (f) EDS maps of HAZR of double-pass FSWed joints

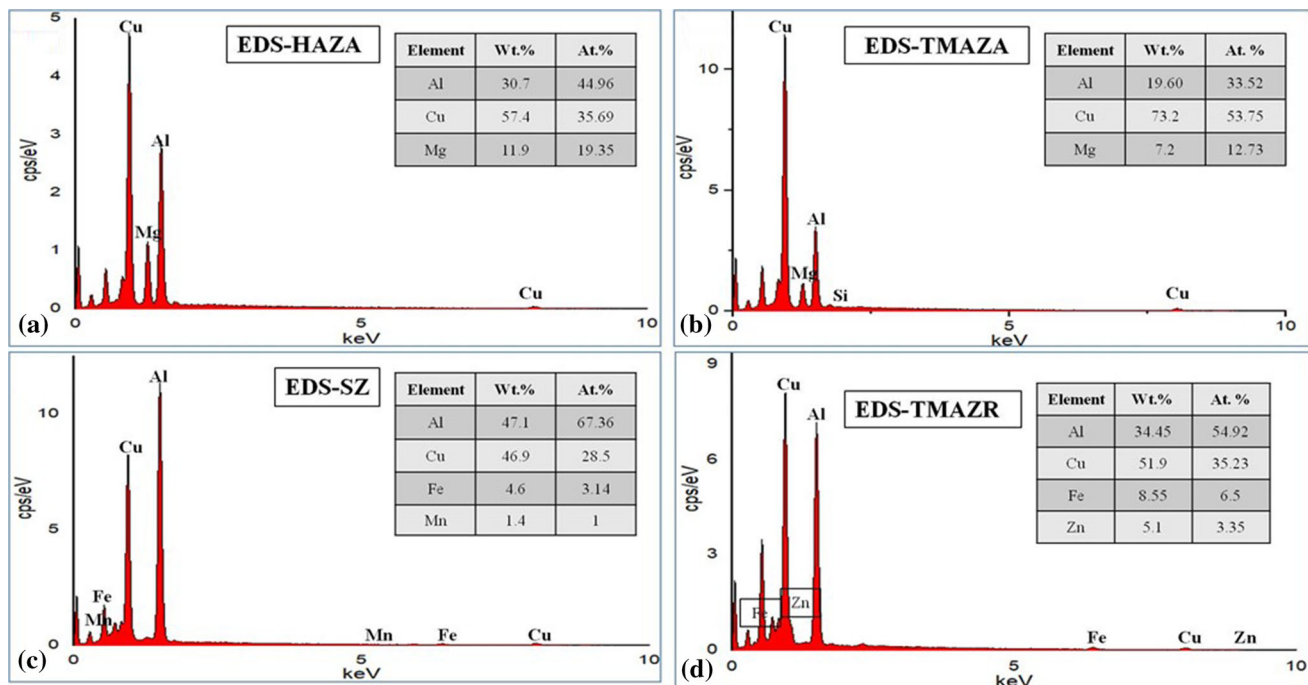


Fig. 10 EDS elemental maps of (a) HAZA, (b) TMAZA, (c) SZ and, (d) TMAZR of double-pass FSWed joints

weld while these second phase coarse particles were finer and uniformly distributed in double-pass weld owing to proper mixing and dynamic breakdown of precipitates formed during first pass. Moreover, x-ray EDS analysis of second phase precipitates reveals the formation of different second phase particles in double-pass joint in comparison to those formed in single-pass joint. The coarse second phases (Table 4) evolved in TMAZA and HAZA during double-pass (refer Fig. 9b) were relatively large as compared to that formed in TMAZA and HAZA of single-pass joint (refer Fig. 7b), which is attributed to the increasing effect of thermal cycles in double-pass. Whereas relatively coarse second phase precipitates were obtained in TMAZR and HAZR of double-pass FSW weld as compared to single-pass FSW weld; due to increased heat input across the weld cross section during double-pass FSW (Ref 22, 23). Additionally, the difference in size between the coarse second phase particles on AS and RS is due to the presence of dissimilar alloys across the weld centerline. Thus, it can be concluded that double-pass FSW leads to change in size and chemical composition of precipitates owing to change in thermal history and mechanical deformation of pre-welded material by double-pass FSW. In addition, irrespective of the nature of the precipitates and number of passes, the precipitates are relatively coarse in HAZA as compared to HAZR due to high heat input on AS leading to the subsequent reduction in joint hardness and strength.

3.3 Microhardness

The 2D Vickers microhardness maps across the weld cross section are shown in Fig. 11. Figure 11(a) and (b) illustrates the hardness profiles of single and double-pass welds. The hardness values were measured at three different locations, i.e., the bottom of weld, the center of thick plate, and parallel to weld (Fig. 2). Drastic variations in the microhardness within the weld region were due to non-homogeneous microstructure across the weld cross section. Irrespective of single and double-pass, it was observed that the hardness of the top layer was higher than the middle and bottom layer (refer Fig. 11) due to high heat and dynamic recrystallization of material underneath the tool shoulder. Moreover, it can be noticed that in both single-pass and double-pass joints, higher hardness values were observed in SZ (fine grains) due to intense plastic deformation and dynamic recrystallization of grains. The hardness value decreases as one move through TMAZ to HAZ due to coarsening of grains and softening of precipitates by thermal cycles. The minimal hardness values were associated with HAZ on the AS. This decrease in hardness values was due to the softening and coarsening of strengthening precipitates as a result of increased heat input on AS during welding (Ref 24).

Moreover, the reduction in hardness was more dominant on the AS than RS which may be attributed to the presence of lower strength alloy (AA2024-T3) on AS and due to increased heat input on AS in comparison to RS (Ref 25).

It is clear from Fig. 11(b) that the average hardness value decreased in subsequent double-pass. The effect of reduction in hardness value was more prominent in HAZ than TMAZ followed by SZ. The hardness decreased significantly on AS in comparison to RS in HAZ during the double-pass. This condition was attributed to the more heat on AS than on RS which consequently leads to further coarsening of precipitates formed during single-pass. It can also be depicted from SEM maps that significant coarsening of precipitates in HAZ and TMAZ on AS (Fig. 7 and 9) has occurred. Dissolution and coarsening of precipitates were observed on RS in TMAZ and HAZ. This coarsening and softening of precipitates caused decrease in hardness and joint strength. The effect of reduction in hardness values in SZ in double-pass was not much dominant due to increased recrystallization of grains in double-pass. However, the dissolution of precipitates in SZ (Fig. 9) of double-pass weld has resulted in a subsequent reduction in hardness values.

3.4 Tensile Strength

The ultimate tensile strength (UTS), percentage elongation, and joint efficiency of single-pass and double-pass joints are given in Table 5. Figure 12 represents the variation of joint properties in single and double-pass welds. The UTS, joint efficiency, and percentage elongation of single-pass joint were found to be 387.6 MPa, 82.8%, and 20.38%, respectively. Whereas the UTS, joint efficiency and percentage elongation of double-pass joint were found to be 364.9 Mpa, 78%, and 18.14 %, respectively (Table 5). Lower strength of the joints than BMs was due to change in the chemistry and thermal history of material during FSW. Furthermore, it can be revealed from experimental results that joint strength, ductility, and joint efficiency decreased in double-pass joints. The reduction in strength of double-pass was due to the thermal softening/annealing or overaging of strengthening precipitates (in TMAZ and HAZ) caused by increased heat input during the double-pass. Moreover, during the double-pass, the tool shoulder was in proper contact with the pre-welded joint surface and the whole heat input during the double-pass resulted in the softening effect of strengthening precipitates particularly in the HAZ as the lowest joint strength region. Additionally, there is a corresponding decrease in joint ductility by 2.64% (Fig. 12) by double-pass FSW. The reduction in ductility may be attributed to the increased strain hardening during the double-pass. Furthermore, it can be observed from Table 5, that the

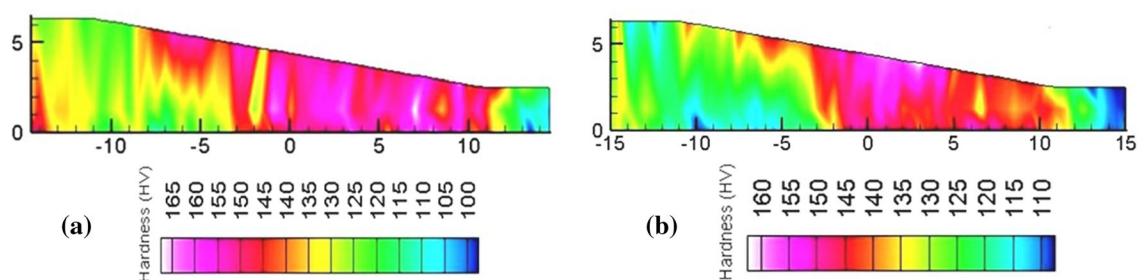


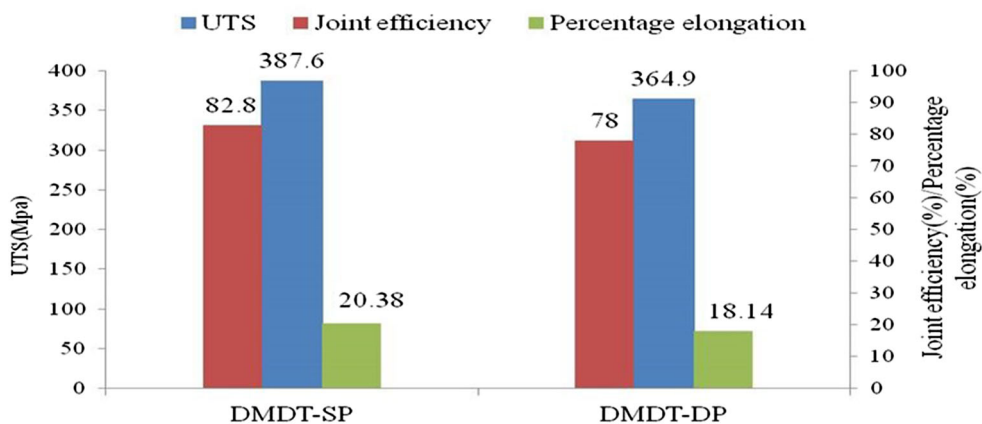


Fig. 11 Vickers microhardness maps of (a) Single-pass, and (b) Double-pass FSW of TWBs

Table 5 Ultimate tensile strength, percentage elongation, joint efficiency, and fracture location of tensile specimens

Specimen Name	UTS, MPa	Elongation, %	Joint efficiency, %	Fractured specimens	Fracture location
DMDT-SP	387.6	20.38	82.8		Outside the joint
DMDT-DP	364.9	18.14	78		HAZ

**Fig. 12** Variation of mechanical properties of the joint in single and double-pass FSW

tensile specimen fails in the BM (AA7475-T7) in the case of single-pass weld is attributed to the change in thermal history in BM adjacent to joint region caused by heat conducted to the BM during welding whereas the failure occurred in HAZ on RS (AA7475-T7) in the case of double-pass weld. The cause of failure in HAZ in double-pass weld was attributed to mismatch in thickness between the plates on the AS and RS, and coarsening of grains/overaging of precipitates in HAZ.

3.5 Fracture Surface Analysis

The fracture surface of all joints was observed using SEM micrographs to analyze the failure behavior under tensile loading. Fractography of fractured single-pass and double-pass joints is shown in Fig. 13 and 14, respectively. It can be depicted from Table 5 that the single-pass joint fractured outside the weld, i.e., in the BM (AA7475-T7) while the double-pass joint fractured in HAZ on RS. The failure in HAZ is due to high thermal cycles by double-pass which caused coarsening of grains and overaging of strengthening precipitates and consequently a lower joint strength region (HAZ). Figure 13(a) shows the fractured surface of single-pass joint. It can be observed that the specimens fractured in steps due to reasonable differences in thickness between the plates (Fig. 13a). The higher magnification images (Fig. 13b) appeared rough and uneven indicating cleavage fracture. Furthermore, the presences of large spheroid-shaped precipitates (Fig. 13b) were due to the heat conducted to BM (AA7475-T7) during FSW. Figure 13c illustrates the presence of small and large dimples which characterize ductile fracture. On the other hand, the presence of tearing edges (indicated with yellow arrows) is characteristic of brittle fracture. Thus, it can

be concluded that a mixed mode of failure (both ductile and brittle) known as the quasi-cleavage fracture was observed in single-pass joint.

Figure 14(a) shows the fractured surface of tensile specimen after failure in double-pass FSW. From Fig. 14(b), the fractured surface shows ridges which are the typical characteristic of brittle fracture. However, the presence of small dimples on the lower side (Fig. 14b) indicates the ductile mode of fracture. It can also be absorbed in Fig. 14(c); the fractured surfaces reveal the existence of small and large dimples; and small cracks indicating the typical ductile mode of failure. The dimples are produced owing to the coalescence of small and large voids leading to ductile and brittle fracture. The presence of large dimples indicates the overloading and ductile nature of the failure. In addition, the presence of coarse second phase precipitates on the bottom of dimples and tearing edges indicates the micro-cracks have nucleated from coarse second phase precipitates in TMAZ and ultimately leading to gradual fracture under plastic deformation (Ref 26). Thus, it can be inferred that the nature of failure in both single-pass and double-pass FSW is the quasi-cleavage mode of failure.

3.6 Thermal Analysis

Thermal profiles at several locations across the weld centerline (Fig. 15) were acquired by eight K-type thermocouples (T_1 to T_8) to analyze the effect of temperature and thermal cycles on the mechanical performance of joint during single and double-pass FSW. However, for convenience and to explain the results more precisely, the temperature readings of only two thermocouples (T_2 on AS and T_8 on RS) were considered installed at the midway at a distance of 2 mm from

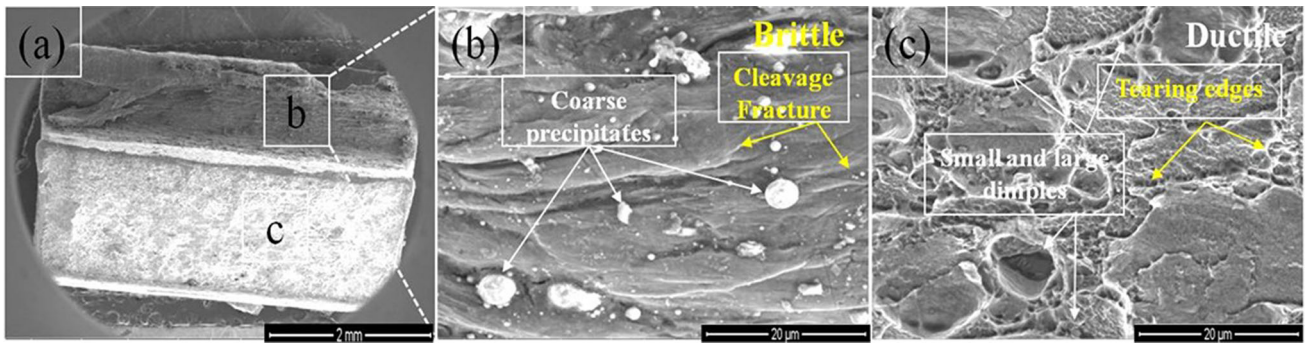


Fig. 13 SEM images showing (a) Fractured tensile surface, (b) Brittle mode of fracture, and (c) Mixed mode of fracture in single-pass FSW Specimen

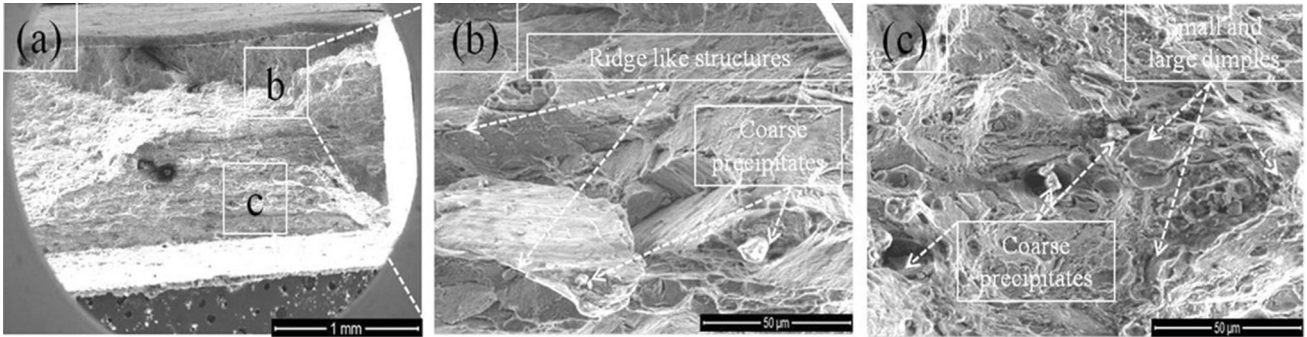


Fig. 14 SEM images showing (a) Fractured tensile surfaces, (b) Brittle mode of fracture, and (c) mixed mode of fracture in double-pass FSW specimens

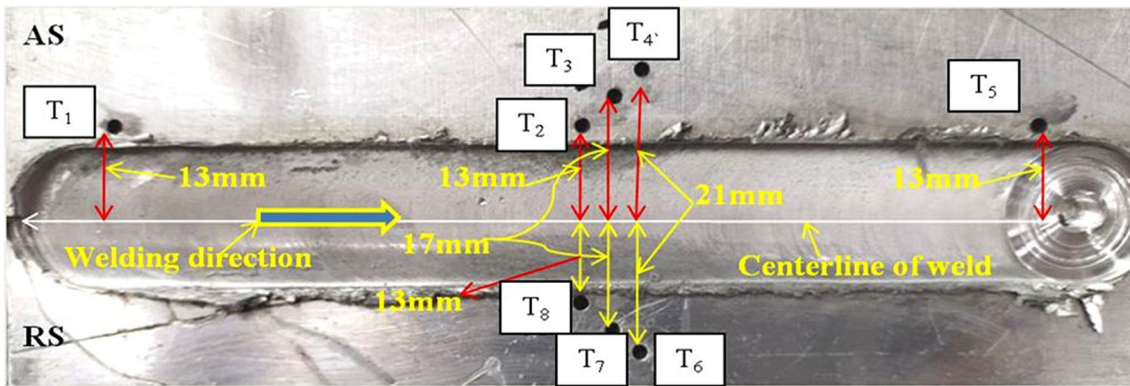


Fig. 15 Location of thermocouples installed to acquire temperature data

the tool shoulder periphery on either side of the weld centerline as illustrated in Fig. 15. Figure 16(a) and (b) illustrates the thermal plots that shows the same trend on AS and RS of the joint in single-pass and double-pass FSW of TWBs, respectively. Figure 16(c) indicates the variation of temperature on AS and RS in single and double-pass FSW. Figure 16(a) and (b) also reveals that temperature profiles are steeper on AS in comparison to RS in both single and double-pass which depicts to the large temperature rise on AS. The peak temperatures evaluated on AS and RS in single-pass joint was found to be 476 °C and 409.25 °C, respectively, whereas the values of peak temperatures on AS and RS in double-pass joint were 369.5 °C and 358.38 °C, respectively. Therefore, in both single and

double-pass joints with thicker plate on the AS, the temperature on AS was higher than on RS due to higher relative volumetric flow rate between the workpiece and tool on the AS (Ref 27). It was also observed that peak temperature (476 °C on AS and 409.25 °C on RS) of single-pass weld was more than double-pass weld (369.5 °C on AS and 358.38 °C on RS). This may be attributed to the formation of step (due to unequal thickness) during single-pass causing more resistance to tool movement and the corresponding increase in heat input. The lower temperature in double-pass weld may be due to the lower frictional contact between the shoulder and pre-finished weld surface (in first pass). However, the temperature difference (refer Fig. 16c) on AS and RS in double-pass weld (11.2 °C)

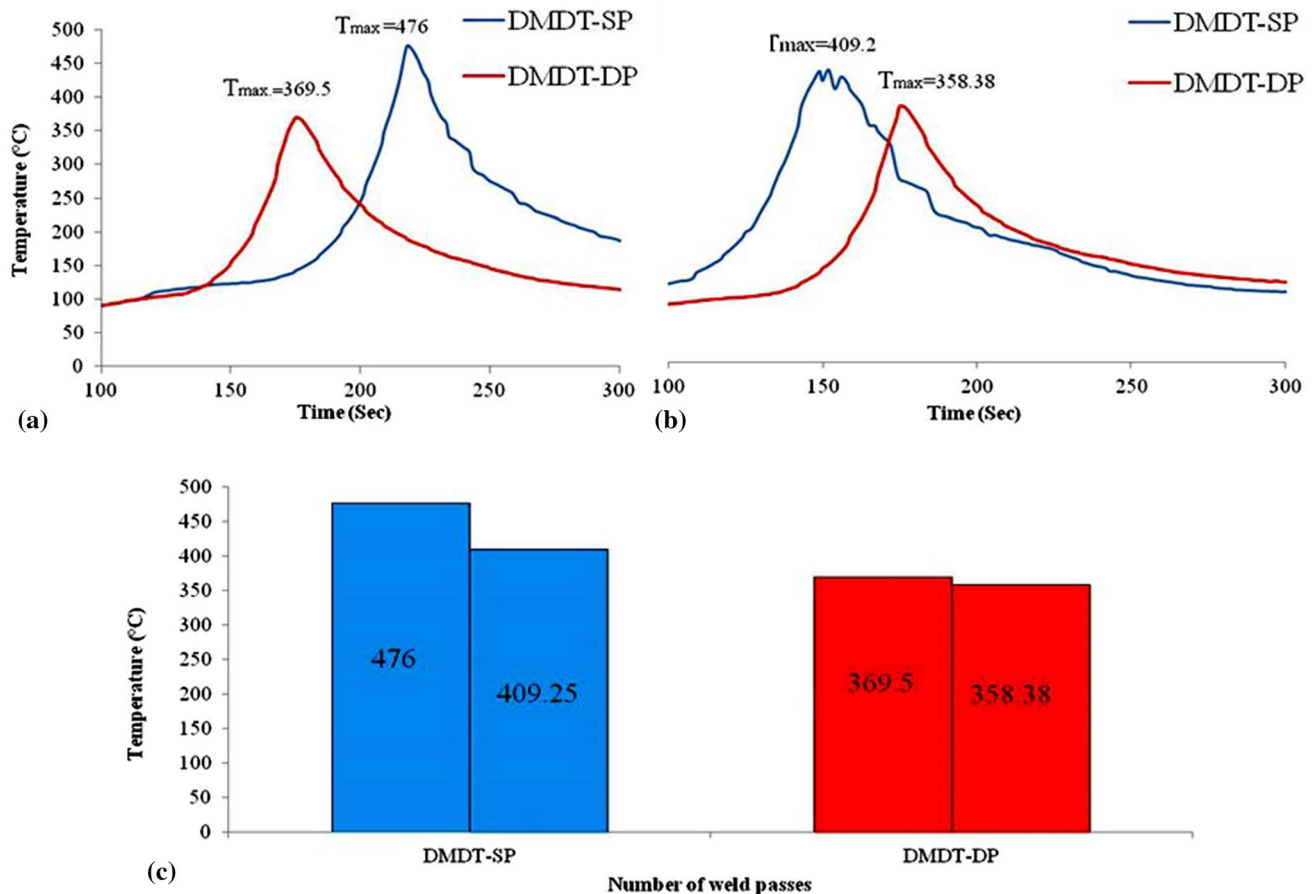


Fig. 16 Temperature profiles (a) Advancing side and (b) Retreating side and (c) temperature rise during the single-pass and double-pass FSW

was lower as compared to single-pass weld (66.75 °C). This condition may be attributed to the fact that during double-pass FSW the tool is in proper contact with the pre-welded surface resulting in more or less uniform heat input on AS and RS.

3.7 Traverse Load Analysis

Figure 17 illustrates the variation of traverse load (F_x) with the distance traveled by the tool during FSW in a single-pass and double-pass welds. The F_x plot rises sharply in the beginning and stabilizes as the tool advances along the welding direction. This rise, in the beginning, is due to lower initial heat input and consequently higher resistance to tool movement (Fig. 17a). As the tool advances, the preheat increases and softens the material ahead of the tool lead to stabilize the F_x . On completion of welding, the tool is stopped and subsequently removed out of the weld causing the F_x to fall to zero. Moreover, the small fluctuation of load in the stabilized portion during welding is attributed to the stick-slip conditions as was observed by Lienert et al. (Ref 28). The high heat generated beneath the shoulder facilitates more softened material leading to a sudden reduction in F_x . Subsequently, as the tool advances, it was encountered by more viscous material leads to increasing resistance to tool advance and corresponding sudden increase in F_x . This cyclic fluctuation of load continued till the completion of welding. Figure 17(b) represents the average value of F_x encountered during the single-pass and double-pass weld. The average value of F_x during a single-pass was found to be

1315.367 N whereas the average value of F_x attained during double-pass was found to 1546.942 N (refer Fig. 17b). Moreover, the peak temperature (i.e., on AS) during single-pass and double-pass was found to be 476 °C and 369.5 °C, respectively (refer Fig.16). Thus, it can be inferred that resistance to tool movement (F_x) is inversely related to temperature rise, i.e., the high heat input causes more softening of material ahead of the tool leading to lower resistance to tool movement whereas low heat input reduces the softening effect leading to higher resistance to tool movement. Furthermore, it can be observed from Fig. 17 that resistance to tool movement is more in a double-pass in comparison to single-pass FSW. This may be attributed to the lower temperature (369.5 °C) during double-pass FSW in comparison to higher temperature rise (476 °C) in a single-pass. In addition, in double-pass, the tool has to move through the intensively deformed and dynamically recrystallized WN produced by a single-pass, further increases the resistance to tool movement and a consequent increase in F_x .

4. Conclusion

In the present experimental study, TWBs of dissimilar aerospace grade Al alloys (AA2024-T3 and AA7475-T7) were joined by FSW in a single-pass and double-pass combinations. The effect of double-pass FSW on mechanical properties of

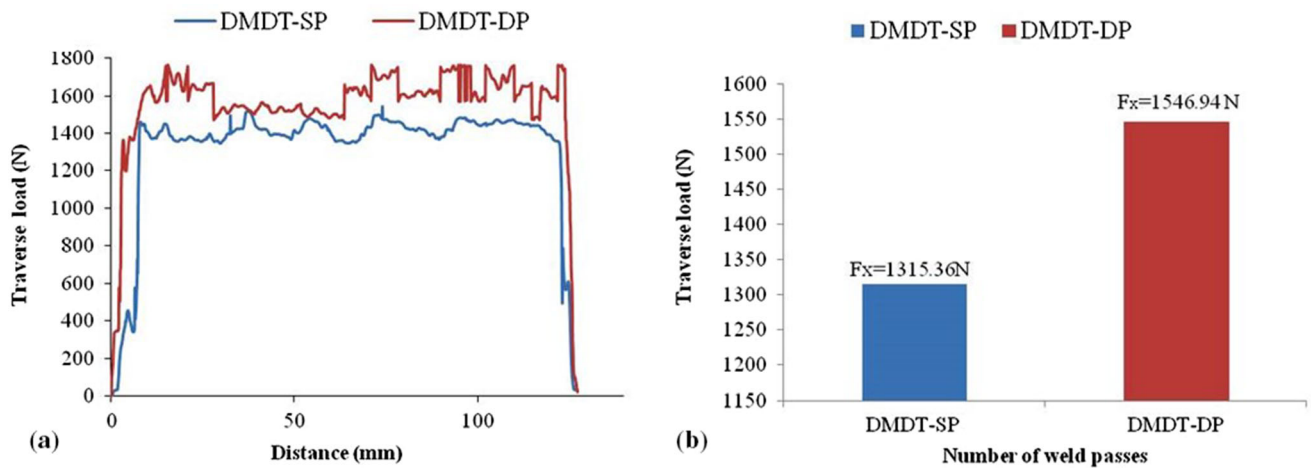


Fig. 17 (a) Traverse load profiles, and (b) The variation of transverse load with the number of welds passes during single and double-pass FSW

joints and; nature and distribution of precipitates in different weld zones were characterized through microhardness, SEM, and x-ray EDS analysis. Based on the experimental results obtained, the following conclusions can be drawn:

1. Defect-free joints were successfully fabricated by FSW between AA2024-T3 alloy (6.35 mm thick) and AA7475-T7 alloy (2.5 mm thick) in both single and double-pass combinations at constant FSW process parameters.
2. Fine and equiaxed grains were observed in WN as compared to TMAZ and HAZ. Moreover, the grain size was found to be bigger in all weld zones across the joint cross section in a double-pass as compared to the single-pass joint.
3. Fine precipitates were observed in WN along the grain boundaries whereas reasonably coarse precipitates were found in TMAZ and HAZ. Relatively large precipitates were observed in double-pass joint than single-pass joint. The nature and size of precipitates reasonably varied in single and double-pass joints due to different thermal history and mechanical forces encountered during the welding process.
4. The microhardness observations reveal higher hardness values at the top layer of the weld than the middle and bottom layers of the weld in both single and double-pass FSW. The overall hardness values decreased by double-pass with major hardness reduction in HAZ on AS.
5. Double-pass tensile specimen displays low tensile strength than single-pass joint due to softening and coarsening of precipitates by double-pass FSW. The tensile samples fail on RS of weld irrespective of the single and double-pass due to significant difference in thickness (3.85 mm) of the alloys on AS and RS. Moreover, the failure of the double-pass specimen in HAZ on RS is attributed to the formation of more coarse grains/precipitates in this joint rejoin.
6. Both ductile and brittle fractures known as “quasi-cleavage” fracture were observed in single and double-pass joints. However, double-pass specimen is less ductile as compared to single-pass specimen.

7. The temperature characterization reveals the lower temperature rise in a double-pass in comparison to a single-pass. Moreover, the difference in temperatures on AS and RS by double-pass was lower than a single-pass FSW.
8. The traverse force (F_x) was significantly increased by double-pass FSW due to lower heat input during welding. Moreover, it is observed that F_x is inversely related to heat input and is independent of the number of FSW passes.

References

1. P.A. Schweitzer, Aluminum and Aluminum Alloys, *Met. Mater. Phys. Mech. Corros. Prop.*, 2003 <https://doi.org/10.1201/9780203912423.ch19>
2. A.K. Jha, P.R. Narayanan, V. Diwakar, K.S. Kumar and M.C. Mittal, Metallurgical Analysis of Cracked Aluminum Alloy (AFNOR 7020) Components Used in Satellite Launch Vehicles, *Eng. Fail. Anal.*, 2004, **11**, p 463–474. <https://doi.org/10.1016/j.engfailanal.2003.05.016>
3. K.V. Jata, K.K. Sankaran and J.J. Ruschau, Friction-Stir Welding Effects on Microstructure and Fatigue of Aluminum Alloy 7050–T7451Metal, *Mater. Trans. A*, 2000, **31A**, p 2181–2192.
4. S.N.J. Reddy, R. Sathiskumar, K.G. Kumar, S. Jerome, A.V. Jebaraj, N. Arivazhagan et al., Friction Based Joining Process for High Strength Aerospace Aluminium Alloy, *Mater. Res. Expr.*, 2019, **6**, p 0863–0865.
5. M. Ubaid, D. Bajaj, A.K. Mukhopadhyay and A.N. Siddiquee, Friction Stir Welding of Thick AA2519 Alloy: Defect Elimination, Mechanical and Microstructural Characterization, *Metals Mater. Int.*, 2020, **26**, p 1841–1860.
6. E.C. Bonome, C.B. Carletti, N.G.D. Alcantara and J.F.D. Santos, Friction Stir Welding Applied to Tailored Blanks, *Weld. Inter.*, 2007, **21**(4), p 279–283.
7. P. Rohilla and N. Kumar, Experimental Investigation of Tool Geometry on Mechanical Properties of Friction Stir Welding of AA6061, *Int. J. Innov. Technol. Expl. Eng. (IJITEE)*, 2013, **3**, p 2278–3075.
8. N.A.A. Sathari, L.H. Shah and A.R. Razali, Investigation of Single-Pass/Double-Pass Techniques on Friction Stir Welding of Aluminium, *J. Mech. Eng. Sci. (JMES)*, 2014, **7**, p 1053–1061. <https://doi.org/10.15282/jmes.7.2014.4.0102>
9. G. Ghangas and S. Singhal, Investigations of Multi-Pass Friction Stir Welding for Al-Zn-Mg alloy, *Mater. Today: Proc.*, 2018, **5**, p 17107–17113.

10. R. Brown, W. Tang and A.P. Reynolds, Multi-Pass Friction Stir Welding in Alloy 7050–T7451: Effects on Weld Response Variables and on Weld Properties, *Mater. Sci. Eng. A*, 2009, **513**, p 115–121.
11. S. Gopi and K. Manonmani, Predicting Tensile Strength of Double Side Friction Stir Welded 6082–T6 Aluminium Alloy, *Sci. Technol. Weld. Join.*, 2012, **17**(7), p 601.
12. S. Mehra, P. Dhanda, R. Khanna, N. Singh Goyat and S. Verma, Effect of tool on tensile strength in single and double sided friction stir welding, *Int. J. Sci. Eng. Res.*, 2012, **3**, p 11.
13. N.H. Othman, L.H. Shah and M. Ishak, Mechanical and microstructural characterization of single and double pass aluminum AA6061 friction stir weld joints, Dec 2015. 3rd international conference of mechanical engineering research, IOP Conference Series: Materials Science and Engineering, 2015. <https://doi.org/10.1088/1757-899X/100/1/012016>
14. M. Muzvidziwa, M. Okazaki, S. Yamagishi and M. Seino, Local Fatigue Crack Propagation Behavior of a Two-Pass Friction Stir Welded Aluminum Alloy, *Mech. Eng. J.*, 2014, **1**, p 6
15. A. Kar, S. Suwas and S.V. Kailas, Two-Pass Friction Stir Welding of Aluminum Alloy to Titanium Alloy: A Simultaneous Improvement in Mechanical Properties, *Mater. Sci. Eng. A*, 2018 <https://doi.org/10.1016/j.msea.2018.07.057>.PII
16. A. Garg and A. Bhattacharya, Influence of Cu Powder on Strength, Failure and Metallurgical Characterization of Single, Double pass Friction Stir Welded AA6061-AA7075 Joints, *Mater. Sci. Eng., A*, 2019, **759**, p 661–679.
17. N. Gangil, S. Maheshwari and A.N. Siddiquee, Novel use of Distribution Facilitators and Time–Temperature Range For Strengthening in Surface Composites on AA7050-T7451, *Metallogr., Microstruct. Anal.*, 2018, **7**(5), p 561–577.
18. P. Kumar Sahu and S. Pal, Mechanical Properties of Dissimilar Thickness Aluminium Alloy weld by Single/Double pass FSW, *J. Mater. Process. Technol.*, 2017 <https://doi.org/10.1016/j.jmatprotec.2017.01.009>
19. T. Majeed and Y. Mehta, Arshad Noor Siddiquee, *Proc. IMechE Part L: J Mater.: Design Appl.*, 2021, **235**(4), p 934–945.
20. N. Birbilis, M.K. Cavanaugh and R.G. Buchheit, Electrochemical Behavior and Localized Corrosion Associated with Al₇Cu₂Fe Particles in Aluminum Alloy 7075–T651, *Corros. Sci.*, 2006, **48**, p 4202–4215. <https://doi.org/10.1016/j.corsci.2006.02.007>
21. D. Bajaj, A.N. Siddiquee, A.K. Mukhopadhyay and N. Ali, The Effect of Tool Design on the Friction Stir Welding of Thick Aluminum Alloy AA6082-T651 Extruded Flats, *Metallogr., Microstruct. Anal.*, 2020, **9**, p 841–855.
22. W.P. Koster, in *Aluminium Alloys, ASM Handbook*, 9th edn. Metallography and Microstructure, vol 9 (The ASM Handbook Committee, ASM International, 1992), p 351–388
23. M. Starink and X. Li, A model for the Electrical Conductivity of Peak-Aged and Overaged Al-Zn-Mg-Cu alloys Metall, *Mater. Trans. A*, 2003, **34**, p 899–911.
24. G. Cam, S. Gucluer and A. C. akan and H. Serindag, ‘Mechanical Properties of Friction Stir Butt-Welded Al-5086 H32 plate’, *Materialwiss, Werkstofftech*, 2009, **40**, p 638–642.
25. C. Menzemer and T. Srivatsan, The Effect of Environment on Fatigue Crack Growth Behavior of Aluminum Alloy 5456’, *Mater. Sci. Eng. A*, 1999, **A271**, p 188–195.
26. W.S. Huang, J.H. Chen, H.G. Yan, W.J. Xia, B. Su and W.J. Zhu, Effects of Ga Content on Dynamic Recrystallization and Mechanical Properties of High Strain Rate Rolled Mg-Ga Alloys, *Met. Mater.-Int.*, 2019, **26**(6), p 747–759.
27. H. Mohanty, M.M. Mahapatra, P. Kumar, P. Biswas and N.R. Mandal, Study on the Effect of Tool Profiles On Temperature Distribution and Material Flow Characteristics In Friction Stir Welding, *IMech E Part B: J Eng Manuf*, 2012, **226**(9), p 1527–1535.
28. T.J. Lienert, W.L. Stellwag Jr., B.B. Grimmer and R.W. Warke, Friction Stir Welding Studies on Mild Steel, *Weld J-New York*, 2003, **82**(1), p 1–8.

Publisher's Note Springer Nature remains neutral with regard to jurisdictional claims in published maps and institutional affiliations.